Monthly Notices
of the
ROYAL ASTRONOMICAL SOCIETY

Mon. Not. R. Astron. Soc. **427,** 3029–3043 (2012) doi:10.1111/j.1365-2966.2012.21945.x

# Discovery of multiphase cold accretion in a massive galaxy at $z = 0.7$

Glenn G. Kacprzak,[1,★†] Christopher W. Churchill,[2‡] Charles C. Steidel,[3] Lee R. Spitler[1] and Jon A. Holtzman[2]

[1] *Centre for Astrophysics and Supercomputing, Swinburne University of Technology, PO Box 218, Victoria 3122, Australia*
[2] *Department of Astronomy, New Mexico State University, Las Cruces, NM 88003, USA*
[3] *California Institute of Technology, MS 105-24, Pasadena, CA 91125, USA*

Accepted 2012 August 15. Received 2012 August 15; in original form 2012 February 28

## ABSTRACT

We present detailed photo+collisional ionization models and kinematic models of the multiphase absorbing gas, detected within the *Hubble Space Telescope*(*HST*)/COS, *HST*/STIS and Keck/HIRES spectra of the background quasar TON 153 at 104 kpc along the projected minor axis of a star-forming spiral galaxy ($z = 0.6610$). Complementary $g'r'i'Ks$ photometry and stellar population models indicate that the host galaxy is dominated by an ∼4 Gyr stellar population with slightly greater than solar metallicity and has an estimated $\log M_* = 11$ and a $\log M_{\rm vir} = 13$. Photoionization models of the low-ionization absorption (Mg I, Si II, Mg II and C III), which trace the bulk of hydrogen, constrain the multicomponent gas to be cold ($\log T = 3.8$–$5.2$) and metal poor ($-2.6 \leq$ [X/H] $\leq 1.32$). A lagging halo model reproduces the low-ionization absorption kinematics, suggesting gas coupled to the disc angular momentum, consistent with cold accretion mode material in simulations. The C IV and O VI absorption is best modelled in a separate collisionally ionized metal-poor ($-2.50 \leq$ [X/H] $\leq -1.93$) warm phase with $\log T = 5.3$. Although their kinematics are consistent with a wind model, given the 2–2.5 dex difference between the galaxy stellar metallicity and the absorption metallicity we indicate that the gas cannot arise from galactic winds. We discuss and conclude that although the quasar sightline passes along the galaxy minor axis at a projected distance of 0.3 virial radii, well inside its virial shock radius, the combination of the relative kinematics, temperatures and relative metallicities indicates that the multiphase absorbing gas arises from cold accretion around this massive galaxy. Our results appear to contradict recent interpretations that absorption probing the projected minor axis of a galaxy is sampling winds.

**Key words:** galaxies: ISM – quasars: absorption lines.

## 1 INTRODUCTION

Over the last decade, simulations have shown that galaxy evolution is highly dependent on gas accretion occurring via two modes: hot and cold accretion. Current cosmological simulations demonstrate that the majority of gas accretion at early epochs on to galaxies occurs via the cold mode, which has temperatures of $T \sim 10^4$–$10^5$ K and metallicities of $Z \lesssim 0.01\,Z_\odot$. Cold-mode gas is preferentially accreted along cosmic filaments/streams and has high densities and low cooling times providing a large supply of gas penetrating through hot haloes surrounding galaxies (Kereš et al. 2005, 2009; Dekel & Birnboim 2006; Ocvirk, Pichon & Teyssier 2008; Brooks et al. 2009; Dekel et al. 2009; Ceverino, Dekel & Bournaud 2010; Faucher-Giguère, Kereš & Ma 2011; Stewart et al. 2011a,b; van de Voort & Schaye 2011; van de Voort et al. 2011). It is expected that cold accretion should comprise no more than 7 per cent of the total H I mass density at $z \sim 1$ (Kacprzak & Churchill 2011).

It is further expected that cold accretion truncates when the host-galaxy mass exceeds $\sim 10^{12}\,M_\odot$, since infalling gas becomes shock-heated to the halo virial temperature ($\sim 10^6$) and is predicted to dramatically reduce the cold accretion cross-section to a tiny fraction (e.g. Kereš et al. 2005, 2009; Dekel & Birnboim 2006; Ocvirk et al. 2008; Brooks et al. 2009; Dekel et al. 2009; Stewart et al. 2011a; van de Voort & Schaye 2011; van de Voort et al. 2011) of the observed halo gas cross-section (Kacprzak et al. 2008; Chen et al. 2010). However, it is expected that these dense filaments can still survive within hot haloes and could provide an efficient means of feeding massive galaxies with pristine gas (e.g. Kereš et al. 2005).

★E-mail: gkacprzak@astro.swin.edu.au
†Australian Research Council Super Science Fellow.
‡Visiting Professor, Swinburne University of Technology, Victoria 3122, Australia.

The study of absorbing foreground gas detected in background quasar spectra allows us to probe these otherwise unobservable comic filaments and outflows. Mg II absorption is ideal for detecting cold-mode and hot-mode accretion, wind outflows, etc., since it probes gas with a large range of neutral hydrogen column densities, $10^{16} \lesssim N(\mathrm{H\,I}) \lesssim 10^{22}$ cm$^{-2}$ (Churchill et al. 2000; Rigby, Charlton & Churchill 2002), with gas temperatures of around 30 000−40 000 K and average total hydrogen densities of ∼0.1 atoms cm$^{-3}$ (Churchill, Vogt & Charlton 2003; Ding, Charlton & Churchill 2005). It has also been thoroughly demonstrated that Mg II absorption is produced within gaseous haloes surrounding galaxies and is not produced within the intergalactic medium (see Churchill, Kacprzak & Steidel 2005).

Over the last decade, strong Mg II absorption has also been observed to directly trace 100–1000 km s$^{-1}$ galactic-scale outflows (Tremonti, Moustakas & Diamond-Stanic 2007; Martin & Bouché 2009; Weiner et al. 2009; Rubin et al. 2010; Coil et al. 2011; Martin et al. 2012) that extend out to at least 50 kpc along the galaxy minor axis (Bordoloi et al. 2012; Bouché et al. 2012; Kacprzak, Churchill & Nielsen 2012). Galactic winds have been observed over a large range of redshifts and detected using a range of ions (see Steidel et al. 2010, and references therein). Correlations between galaxy colours and star formation rates with Mg II equivalent widths also indirectly suggest that absorption is produced in outflows (Zibetti et al. 2007; Noterdaeme, Srianand & Mohan 2010; Nestor et al. 2011).

However, Mg II has been observed infalling (Martin et al. 2012) into highly inclined galaxies with velocities of 100–200 km s$^{-1}$ (Rubin et al. 2012). This is consistent with Kacprzak et al. (2011b) who showed that absorption strength is correlated with the orientation of the galaxy major axis, implying that a significant fraction of weaker Mg II absorption systems are likely accreting towards the galaxy via cold flows. The bimodal azimuthal angle distribution of quasar sightlines around Mg II absorption-selected galaxies also suggests that infall occurs along the projected galaxy major axis (Bouché et al. 2012; Kacprzak et al. 2012). These cold-flow streams likely produce a circumgalactic corotating gas component that is predominately infalling towards the galaxy and, in absorption, these structures are expected to have ∼100 km s$^{-1}$ velocity offsets relative to the host galaxy and in the same direction of galaxy rotation (Stewart et al. 2011b). These models are consistent with previous observations of Steidel et al. (2002) and Kacprzak et al. (2010a) that show Mg II absorption residing fully to one side of the galaxy systemic velocity and usually aligned with the expected galaxy rotation direction, with the absorption essentially mimicking the extension of the galaxy rotation curve out into the halo. We expect low-ionization states, such as Mg I, Mg II, Si II, C II and C III, to be ideal for tracing cold-mode accretion given metallicities, temperatures and densities as expected.

A reliable means of determining the origins of the absorbing gas is to obtain both the host-galaxy and absorption-line metallicity. Absorption-line metallicities for a handful of systems have been determined to range between [M/H] $< -1.8$ and $-1$ while existing near sub-$L^\star$ galaxies that have nearly solar metallicities (Zonak et al. 2004; Chen, Kennicutt & Rauch 2005; Tripp et al. 2005; Cooksey et al. 2008; Kacprzak, Murphy & Churchill 2010b; Ribaudo et al. 2011; Thom et al. 2011). It is postulated that these extremely low metallicity absorption systems are likely accreting on to their host galaxies and possibly trace cold-mode accretion, which is still expected for these sub-$L^\star$ galaxies. The rare case where absorption-line metallicities are larger than those of the host galaxy suggests that the absorption is probing winds (Péroux et al. 2011).

Here we target a particular galaxy that has Mg II absorption consistent with disc-like kinematics, possibly tracing cold accretion. The absorption also contains a separate warm phase as indicated by separate strong C IV absorption that does not coincide with Mg II. We have obtained supplementary *Hubble Space Telescope* (*HST*)/COS data in order to determine the physical properties of the gas. In this paper, we employ kinematic and photo+collisional ionization models of multiphase absorbing gas obtained from *HST*/COS, *HST*/STIS and Keck/HIRES, which is associated with a star-forming spiral galaxy at $z = 0.6610$. In Section 2 we describe our targeted galaxy and our data. We discuss our absorption-line analysis in Section 3. In Section 4 we describe the host-galaxy properties determined from broad-band photometry and stellar population models. In Section 5 we describe the results of our kinematic and photo+collisional ionization models and the physical properties of the absorbing gas. In Section 6, we discuss the possible origins of the absorption, and our concluding remarks are presented in Section 7. Throughout we adopt an $H_0 = 70$ km s$^{-1}$ Mpc$^{-1}$, $\Omega_\mathrm{M} = 0.3$, $\Omega_\Lambda = 0.7$ cosmology.

## 2 TARGET FIELD AND OBSERVATIONS

TON 153, also known as Q1317+227, is a bright ($V = 16.0$ mag) quasar at $z_\mathrm{em} = 1.017$. Inspection of a low-resolution quasar spectrum revealed two Mg II absorption systems at $z_\mathrm{abs} = 0.29$ and 0.66 (Steidel & Sargent 1992). Following a spectroscopic survey of galaxies in close angular proximity to the quasar sightline, Steidel et al. (2002) discovered galaxies G1 and G2 shown in Fig. 1. The quiescent early-type galaxy G1 has a redshift of $z_\mathrm{gal} = 0.6719$, and the star-forming disc galaxy G2 has a redshift of $z_\mathrm{gal} = 0.6610$. Churchill et al. (2007) demonstrated that G1 was associated with a Ly$\alpha$ complex that did not have any observable metals even though it resides at $D = 58.1$ kpc, well within the 100 kpc where metals are expected (e.g. Chen, Lanzetta & Webb 2001; Kacprzak et al. 2008; Chen et al. 2010; Tumlinson et al. 2011). In a companion paper (Churchill et al. 2012b), we further discuss G1 and its associated absorption lines. The galaxy G2 is at $D = 103.9$ kpc and is associated with extensive metal-line/LLS absorption at $z_\mathrm{abs} = 0.6601$ (Steidel & Sargent 1992; Bahcall et al. 1993, 1996; Churchill et al. 2000, 2007; Ding et al. 2005), and is the focus of this paper.

### 2.1 *HST* imaging

In Fig. 1 we present a 4700 s *HST*/Wide Field Planetary Camera 2 (WFPC2) F702W image (PID 5984; PI Steidel) that was reduced using the WFPC2 Associations Science Products Pipeline (WASPP[1]). Note that the F702W filter provides a bandpass similar to a rest-frame Johnson *B*-band filter for galaxies at $z \sim 0.6$. Galaxy magnitudes and luminosities were obtained from Churchill et al. (2012a) and are based on the AB system. The GIM2D software (Simard et al. 2002) was used to obtain quantified galaxy morphological parameters that were published in Kacprzak et al. (2011b) and Churchill et al. (2012a).

### 2.2 Ground-based imaging

To further constrain the properties of G2, we analysed multiband $g'r'i'$ and *Ks* imaging. The $g'r'i'$ bands were obtained using an SPIcam CCD imager on the APO 3.5-m telescope. SPIcam has a

[1] http://archive.stsci.edu/hst/wfpc2/pipeline.html

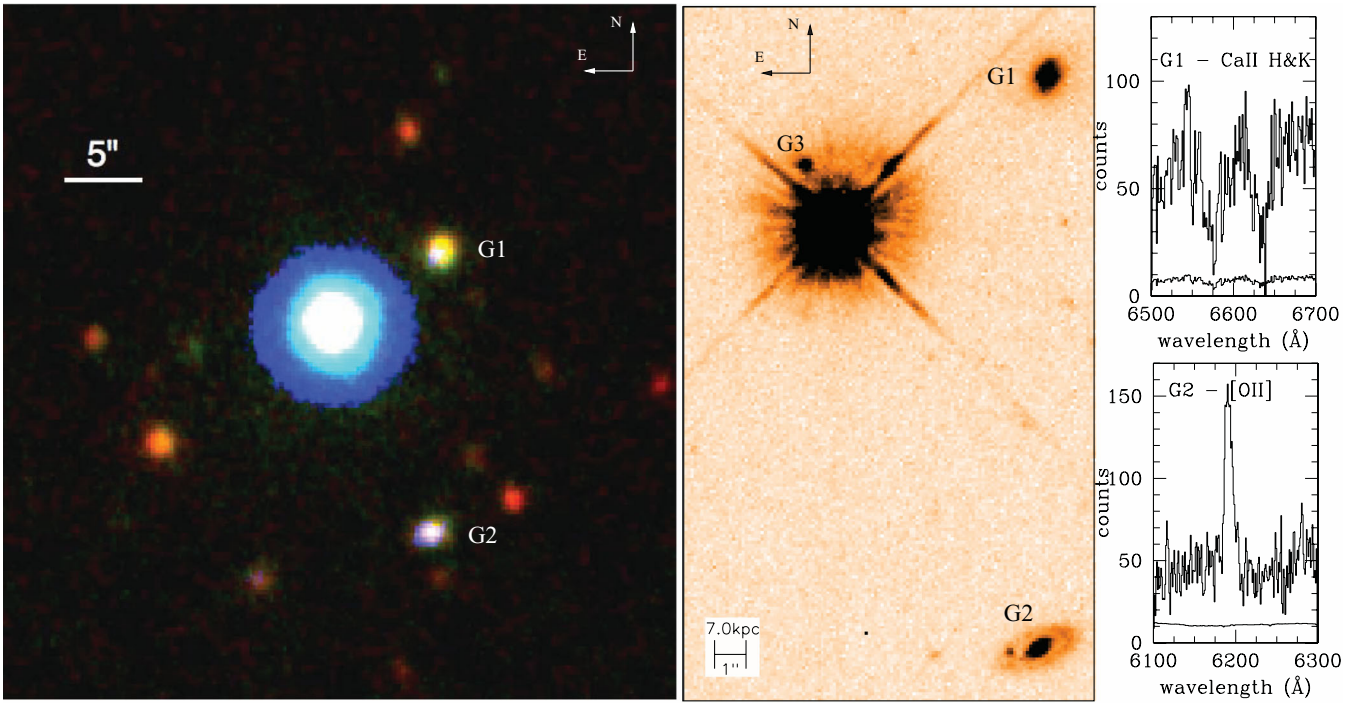


**Figure 1.** Left: ground-based $g'$-band (blue), $i'$-band (green) and *Ks*-band (red) colour composite centred on the quasar. Note that G1 is redder than G2 (see Churchill et al. 2012b). Also note that the surrounding galaxies in the field are extremely red compared to $z \sim 0.6$ galaxies, indicating that they are at much higher redshifts and not associated with the absorption. Middle: a 13 arcsec × 22 arcsec *HST*/Wide Field Planetary Camera 2 (WFPC2) F702W image of the quasar field TON 153. The quasar is the brightest object in the north-east corner of the image. G2 is associated with a variety of metal lines shown in Fig. 2. A possible object seen within ∼1 arcsec north-east of the quasar (G3) has not been successfully identified spectroscopically since the quasar is bright. Note that the quasar sightline passes near the minor axis of the moderately inclined disc of G2. Top-right: a Keck/LRIS spectrum of G1 containing Ca II H&K confirms the redshift of G1 to be $z_{\rm gal} = 0.6719$. Bottom-left: a Keck/LRIS spectrum of G2 containing [O II] emission confirms the redshift of G2 to be $z_{\rm gal} = 0.6610$.

field of view of 4.78 arcmin × 4.78 arcmin and a spatial resolution of 0.14 arcsec pixel$^{-1}$. Our observations were taken with on-chip binning of 2 × 2 which provides a plate scale of 0.28 arcsec pixel$^{-1}$. The images were taken as part of a large survey programme and were observed over four nights between 2006 March and 2007 March providing total exposure times in the $g'r'i'$ of 5190, 4630 and 4350 s, with a typical seeing of 1.1–1.6 arcsec.

Multiple frames were taken in each filter, and each frame was individually reduced using the standard IDL and IRAF[2] packages. Pixel-to-pixel variations were removed using a combination of dome and twilight sky flat-fields. Due to point spread function/seeing variations over the long exposures, cosmic rays were removed from each frame separately. The SPIcam pixels are sufficiently small that interpolation errors do not lead to significant photometric uncertainties. The astrometry was calibrated by matching field stars from each frame to USNO A2.0 catalogue stars.

The photometric zero-points were established using a number of stars from the SDSS catalogue. Since the APO $g'r'i'$ filter/detector combination does not exactly match that of the SDSS survey, there can exist colour terms between the two systems. We derived these colour terms by analysing the SDSS stellar photometry from over 30 fields and produced a single photometric solution. We adopt the colour term derived from the large set of observations, and the average corrections are of the order of 0.1 mag.

Deep near-infrared (*Ks*) band images were obtained on 1994 February 24 using the Kitt Peak 4-m Mayall telescope and the IRIM NICMOS 3 256 × 256 camera with 0.6 arcsec pixel$^{-1}$. These images were part of a more extensive Mg II galaxy survey of Steidel, Dickinson & Persson (1994). The images were reduced using the contributed IRAF package DIMSUM.[3] The photometric zero-points were established using a number of stars from the 2MASS point-source catalogue (Skrutskie et al. 2006).

In Fig. 1 we present a $g'i'Ks$ colour composite image centred on TON 153 with galaxies G1 and G2 labelled. See the companion paper by Churchill et al. (2012b) for further discussions of the properties of G1. Note that all other objects near the quasar sightline are red compared to the two $z \sim 0.65$ galaxies, indicating that all the other objects are likely at much higher redshifts and that G1 and G2 are likely isolated objects. Churchill et al. (2012b) noted that the *ROSAT* X-ray luminosity limit for this field is four orders of magnitude less than what is expected for cluster centres and is consistent with the expected luminosity for early-type galaxy haloes at $z = 0.67$. In addition, the absorption metallicities determined by Churchill et al. (2012b) for G1, and those found here, are 1–2 dex lower than that expected for the intercluster medium. Thus, it is likely that the absorption does not arise in a cluster environment.

The galaxy G3 is located within ∼1 arcsec north-east of the quasar sightline and has not been successfully identified spectroscopically since the quasar is bright. It is possible that this object is responsible

[2] IRAF is written and supported by the IRAF programming group at the National Optical Astronomy Observatories (NOAO) in Tucson, AZ. NOAO is operated by the Association of Universities for Research in Astronomy (AURA), Inc., under cooperative agreement with the National Science Foundation.

[3] http://iraf.noao.edu/iraf/ftp/contrib/dimsumV3/. DIMSUM was contributed by P. Eisenhardt, M. Dickinson, S. A. Stanford and F. Valdez.

for either the absorption associated with G1, G2, the $z = 0.29$ absorption system, absorption at the quasar redshift or other metal lines identified in this sightline. If G3 is at $z = 0.67$, then Churchill et al. (2012b) estimate its mass to be a factor of 10 less than the mass of G2 and would have a similar metallicity to G2 according to mass–gas metallicity relations (e.g. Savaglio et al. 2005). Thus, if G3 is at the same redshift as of G2, it could be considered as a satellite of G2 and would occupy the same gaseous and dark matter haloes.

Photometry for calibration and science was extracted using SExtractor (Bertin & Arnouts 1996) using the `MAGAUTO` measurements. Corrections for Galactic dust extinction were applied to the galaxies using the dust maps of Schlegel, Finkbeiner & Davis (1998). We obtained final dust-, colour- and seeing-corrected AB magnitudes for G1 of $m_{g'} = 23.43 \pm 0.03$, $m_{r'} = 22.17 \pm 0.03$, $m_{i'} = 21.01 \pm 0.03$ and $m_{Ks'} = 19.4 \pm 0.1$ (Churchill et al. 2012b), and for G2 of $m_{g'} = 23.23 \pm 0.03$, $m_{r'} = 22.32 \pm 0.03$, $m_{i'} = 21.41 \pm 0.03$ and $m_{Ks'} = 19.9 \pm 0.1$.

### 2.3 Galaxy spectroscopy

The galaxies shown in Fig. 1 were spectroscopically identified by Steidel et al. (2002), and their spectra were first presented in Churchill et al. (2007). A possible object seen within ∼1 arcsec from the quasar seen in the image has not been successfully identified spectroscopically since the quasar is bright. The details of the Keck/LRIS spectroscopic observations can be found in Steidel et al. (2002) and Churchill et al. (2007, 2012b). The spectra are both vacuum and heliocentric velocity corrected. Galaxy G1, identified by Ca II H&K absorption, yields a $z_{\rm gal} = 0.6719$, is associated with a broad Ly$\alpha$ complex that spans 1400 km s$^{-1}$ and yet contains only very weak metal lines (Churchill et al. 2007, 2012b). Galaxy G2 was identified by an [O II] emission line, placing it at $z_{\rm gal} = 0.6610$. This galaxy is associated with extensive metal-line/LLS absorption at $z_{\rm abs} = 0.6601$ (Bahcall et al. 1993, 1996; Churchill et al. 2000, 2007; Ding et al. 2005) and is the focus of this paper. We discuss G2's associated metal lines in the next sections.

### 2.4 Quasar spectroscopy

Some of the $z_{\rm abs} = 0.6601$ absorption properties were measured from a 3600 s Keck/HIRES ($R \sim 45\,000$) exposure observed in 1995 January. The details of the observation and data reduction are described in Churchill & Vogt (2001). In addition, a 12 000 s *HST*/STIS E230M ($R \sim 30\,000$) exposure was obtained (PID 8672; PI Churchill) and the data reduction details are found in Ding et al. (2005).

Recent *HST*/COS observations of the quasar ($R \sim 18\,000$) were obtained using the far-ultraviolet (FUV) G160M grating and the near-ultraviolet (NUV) G185M grating (PID 11667; PI Churchill). The FUV observations were centred at 1600 Å and obtained on 2010 June 25 with an exposure time of 12 580 s. The NUV observations consisted of two exposures that occurred on 2010 May 26 and were optimally co-added. The first 5420 s NUV exposure was centred at 1921 Å, and the 4970 s NUV exposure was centred at 1941 Å. The COS spectra were reduced using the standard *HST* IRAF pipeline. All spectra are both vacuum and heliocentric velocity corrected.

It is important to note that the wavelength solutions across these multiple instruments are consistent at the sub-pixel level. This was verified across all spectrographs by centroiding common ionization absorption lines from the data presented here and the data from Churchill et al. (2012b).

Analysis of the absorption profiles was performed using interactive software (see Churchill et al. 1999, 2000; Churchill & Vogt 2001) for local continuum fitting, objective feature identification and measuring absorption properties. Velocity widths and equivalent widths of the absorption systems were measured between the pixels where the equivalent width per resolution element recovered to the $1\sigma$ detection threshold (Churchill et al. 1999).

## 3 QUASAR ABSORPTION-LINE ANALYSIS

In Fig. 2 we present the absorption-line data, and in Table 1 we present the measured equivalent widths and column densities. We discuss below how the column densities and/or limits were computed for each transition. We further discuss how we account for higher redshift hydrogen-line blends that contaminate the O VI λ1032 and C III λ977 transitions (see Fig. 3).

The H I column density adopted from Churchill et al. (2007), obtained by simultaneously fitting the Ly$\alpha$, Ly$\beta$ and Lyman break obtained from an FOS spectrum, was determined to be $\log[N({\rm H\,I})] = 18.3 \pm 0.3$. This is consistent with the results of Rao, Turnshek & Nestor (2006), who fitted only the Ly$\alpha$ line and determined the column density to be $18.57 \pm 0.02$. If we were to use the Rao et al. value, our derived metallicities would decrease by 0.27 dex.

We also note upon analysing the C IV λλ1548, 1550 doublet that we have deemed the reddest component seen in the C IV λ1551 transition, at roughly 80 km s$^{-1}$, to be real and have included it in our analysis. This feature does not appear in the C IV λ1548 line since this region is contaminated by poor sky subtraction. This component was omitted by the analysis of Ding et al. (2005), but included here.

### 3.1 Accounting for blends in O VI λ1032 and C III λ977

Churchill et al. (2012b) performed detailed Voigt profile (VP) fits to the Lyman series, using the *HST*/COS spectra, in order to determine the gas-phase properties of the G1 absorption complex. The VP fits were performed using our own software MINFIT (Churchill & Vogt 2001; Churchill et al. 2003). The *HST*/COS instrumental line spread functions for the spectrograph settings, and also for the observed wavelength of each modelled transition, were computed by interpolating the online tabulated data (Dixon et al. 2010; Kriss 2011).

Churchill et al. (2012b) determined that a portion of the G1 Ly$\beta$ complex was blended with O VI λ1032 associated with G2, while a different portion of the G1 Ly$\gamma$ complex was blended with C III λ977 associated with G2 as shown in Fig. 3 (the full Ly$\beta$ and Ly$\gamma$ complex is not shown since it spans roughly 1400 km s$^{-1}$).

The VP fits of the O VI λ1032 blended portion of the Ly$\beta$ complex were well constrained by the non-blended Ly$\alpha$, Ly$\gamma$, Ly$\epsilon$ and Ly$\zeta$ lines. The VP fits of the C III λ977 blended portion of the Ly$\gamma$ complex were well constrained by the non-blended Ly$\alpha$, Ly$\beta$, Ly$\epsilon$ and Ly$\zeta$ lines. We show the blended and deblended O VI λ1032 and C III λ977 lines in Fig. 3. Given that G1 hydrogen lines are unsaturated and can be well modelled using most of the H I series, we are confident that we have a robust correction for the spectral shape of the O VI λ1032 and C III λ977 lines. Furthermore, these corrections only affect regions redwards of the galaxy systemic velocity.

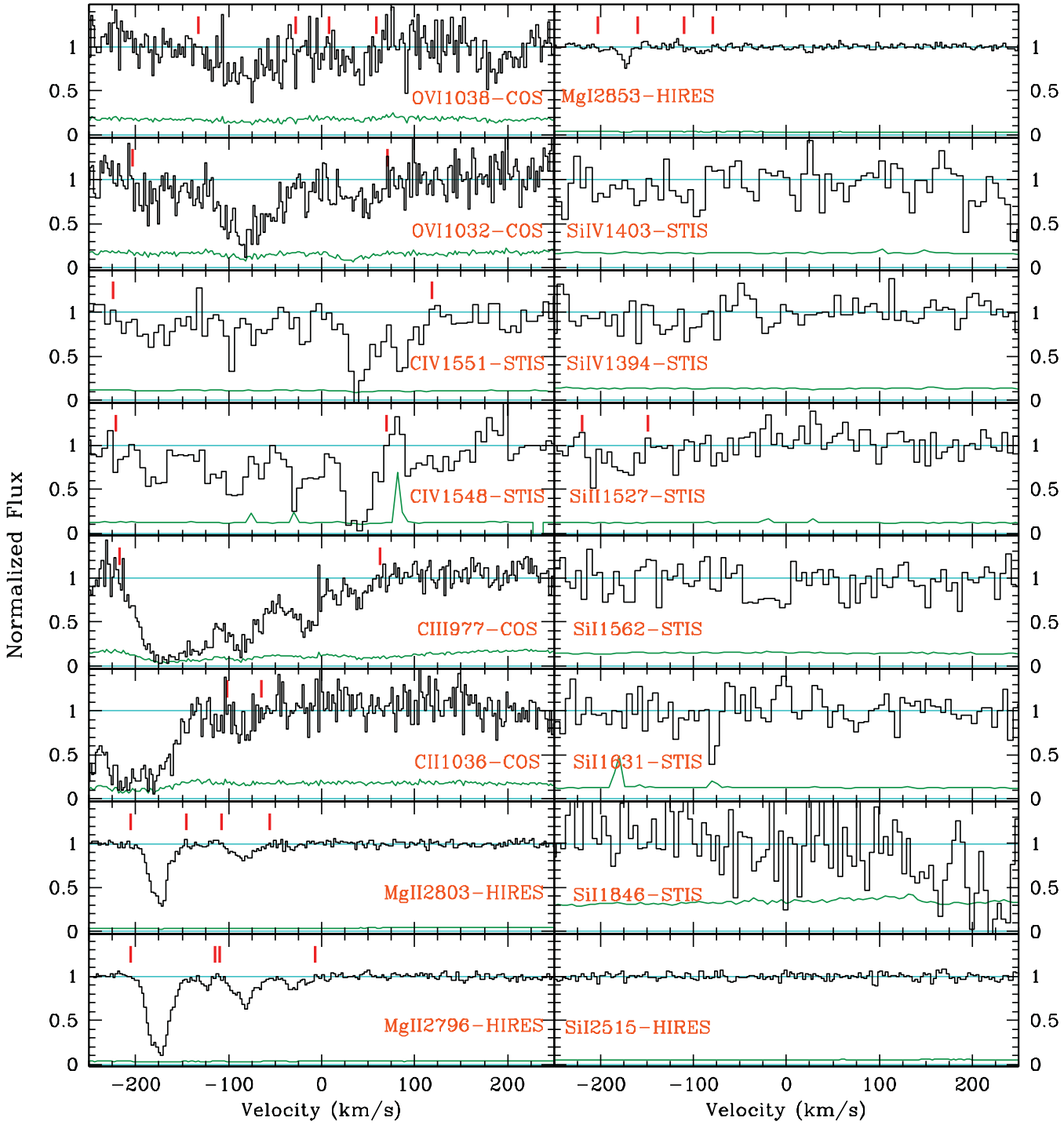


**Figure 2.** Metal absorption lines associated with the $z = 0.6610$ galaxy G2 obtained from *HST*/COS, *HST*/STIS and Keck/HIRES. In each panel the transition and instrument are labelled. The absorption-line data (black) are relative to the systemic velocity of G2. The regions highlighted by the tickmarks (red) indicate the detected absorption features, and the locations of the tickmarks are defined to be where the equivalent width per resolution element recovers to a $1\sigma$ detection threshold. The sigma spectrum is shown below the data (green).

### 3.2 Apparent optical depth method

We employed the apparent optical depth (AOD) method to measure the column densities for each transition using the formalism of Savage & Sembach (1991) and Churchill & Vogt (2001). In the cases where multiple transitions of a given ion were measured, we computed the optimal weighted mean column density in each velocity bin. Since the weighted mean requires the inverse square of the uncertainties, in these cases we treated the non-normal distributions in the uncertainties of the optical depths using the quadratic model of D'Agonstini (2000), D'Agonstini & Raso (2000) and Barlow (2003). The quadratic model approximates the probability distribution of the asymmetric uncertainties in each optical depth data point by a parabola fit to the dimidated Gaussian constructed from

**Table 1.** Absorption properties[a].

| Ion | Instrument/ Telescope | $W_r$ (Å) | $\log N(\mathrm{X})$ | $W_r^{\mathrm{blue}}$ (Å)[b] | [b] $\log N(\mathrm{X})^{\mathrm{blue}}$ | $W_r^{\mathrm{red}}$ (Å)[b] | [b] $\log N(\mathrm{X})^{\mathrm{red}}$ |
|---|---|---|---|---|---|---|---|
| Mg II λ2796 | HIRES/Keck | $0.348 \pm 0.007$ | | $0.348 \pm 0.007$ | | <0.0049 | |
| Mg II λ2803 | HIRES/Keck | $0.198 \pm 0.006$ | | $0.198 \pm 0.006$ | | <0.0060 | |
| Mg II | | | $13.11^{+0.07}_{-0.07}$ | | $13.11^{+0.07}_{-0.07}$ | | ≤11.06 |
| Mg I λ2853 | HIRES/Keck | $0.039 \pm 0.005$ | | $0.039 \pm 0.005$ | | <0.0049 | |
| Mg I | | | $11.54^{+0.06}_{-0.05}$ | | $11.54^{+0.05}_{-0.05}$ | | ≤10.58 |
| Si I λ2515 | HIRES/Keck | <0.0066 | | <0.0066 | | <0.0066 | |
| Si I λ1846 | STIS/*HST* | <0.053 | | <0.053 | | <0.053 | |
| Si I λ1631 | STIS/*HST* | <0.019 | | <0.019 | | <0.019 | |
| Si I λ1562 | STIS/*HST* | <0.023 | | <0.023 | | <0.023 | |
| Si I | | | ≤11.8 | | ≤11.8 | | ≤11.8 |
| Si II λ1527 | STIS/*HST* | $0.067 \pm 0.013$ | | $0.067 \pm 0.013$ | | <0.018 | |
| Si II | | | $13.16^{+0.11}_{-0.08}$ | | $13.16^{+0.11}_{-0.08}$ | | ≤12.6 |
| Si IV λ1394 | STIS/*HST* | <0.019 | | <0.019 | | <0.019 | |
| Si IV λ1403 | STIS/*HST* | <0.023 | | <0.023 | | <0.023 | |
| Si IV | | | ≤12.4 | | ≤12.4 | | ≤12.4 |
| C II λ1036 | COS/*HST* | $>0.018 \pm 0.005$[c] | | $>0.018 \pm 0.005$[c] | | <0.012 | |
| C II | | | $>13.39^{+0.09}_{-0.07}$ | | $>13.39^{+0.09}_{-0.07}$ | | ≤13.1 |
| C III λ977 | COS/*HST* | $0.467 \pm 0.008$ | | $0.431 \pm 0.007$ | | $0.036 \pm 0.004$ | |
| C III | | | $14.20^{+0.03}_{-0.02}$ | | $14.18^{+0.03}_{-0.03}$ | | $12.88^{+0.05}_{-0.05}$ |
| C IV λ1548 | STIS/*HST* | $>0.508 \pm 0.027$[d] | | $0.315 \pm 0.024$ | | $>0.193 \pm 0.031$[d] | |
| C IV λ1551 | STIS/*HST* | $0.417 \pm 0.026$ | | $0.189 \pm 0.021$ | | $0.228 \pm 0.018$ | |
| C IV | | | $14.41^{+0.06}_{-0.05}$ | | $14.11^{+0.07}_{-0.05}$ | | $14.15^{+0.08}_{-0.07}$ |
| O VI λ1032 | COS/*HST* | $0.233 \pm 0.012$ | | $0.189 \pm 0.011$ | | $0.044 \pm 0.006$ | |
| O VI λ1038 | COS/*HST* | $0.105 \pm 0.010$ | | $0.076 \pm 0.008$ | | $0.029 \pm 0.007$ | |
| O VI | | | $14.49^{+0.03}_{-0.03}$ | | $14.33^{+0.04}_{-0.04}$ | | $13.94^{+0.07}_{-0.06}$ |
| H I | FOS/*HST* | | $18.3 \pm 0.3$[e] | | $18.3 \pm 0.3$[e] | | |
| | COS/*HST* | | | | | | $16.03^{+0.18}_{-0.18}$ |

[a]The equivalent width limits are computed at the $3\sigma$ level and are for an unresolved cloud. The column densities are measured using the AOD method, and the column density limits are computed using the COG analysis (see the text).
[b]$W_r$ and $\log N(\mathrm{X})$ are quoted for absorption bluewards ($W_r^{\mathrm{blue}}$) and redwards ($W_r^{\mathrm{red}}$) of the galaxy systemic velocity. The velocity windows used to compute $\log N(\mathrm{X})$ are $-240 \leq v_{\mathrm{abs}} \leq -3\ \mathrm{km\,s^{-1}}$ for gas bluewards of the G2 systemic velocity and $-3 \leq v_{\mathrm{abs}} \leq 220\ \mathrm{km\,s^{-1}}$ for gas redwards of the G2 systemic velocity.
[c]C II is blended with an unknown line at $v_{\mathrm{abs}} < -100\ \mathrm{km\,s^{-1}}$, which is why C II is expressed as a lower limit. The exact value quoted is valid over the velocity window shown in Fig. 2.
[d]C IV λ1551 is affected by poor sky subtraction and is expressed as a lower limit.The exact value quoted is valid over the velocity window shown in Fig. 2.
[e]The H I column density is adopted from Churchill et al. (2007) and was determined by simultaneously fitting the Ly$\alpha$, Ly$\beta$ and the Lyman limit absorption.

the upward and downward measured optical depth uncertainties. Relative to a treatment that neglects the non-normal distribution in the uncertainties, the method effectively provides a point-by-point bias correction to the resulting mean.

In Fig. 4 we present the optimal column density distribution for each transition. The Mg II, C IV and O VI AOD distributions were computed using the doublet. For the C IV λ1548 line, we masked out pixels that were unusable as indicated by the two spikes in the sigma spectrum visible in Fig. 2. Note the difference in the optical depth as a function of the velocity of each transition, especially between Mg II and C IV. We also employed the AOD method to compute the remaining column densities presented in Table 1.

Even though the Lyman series is saturated, we have optimally combined all the series lines to produce the H I column density distribution presented in Fig. 4. Note that some central pixels are saturated and we therefore cannot obtain a total column density; however, we can compute the H I column density over a range of velocity windows where there is no saturation.

### 3.3 Curve of growth analysis

We use the curve of growth (COG) analysis to determine the column density limits of various transitions of silicon and for Mg II, Mg I and C II redwards of the galaxy systemic velocity. The equivalent width limits quoted in Table 1 are $3\sigma$ limits for an unresolved single cloud. The single-cloud assumption for silicon is motivated by the Si II λ1527 absorption line, given that we would likely expect to detect the remaining silicon transition as a single-cloud component consistent with the strongest Mg II cloud located at roughly $-180\ \mathrm{km\,s^{-1}}$.

The measured equivalent width limits are small, and being on the linear part of the COG implies that the column densities are mostly independent of the Doppler parameter ($b$). In fact, for $b \geq 5$, the predicted column densities are independent of $b$. We find that the Si II column density is best constrained by the Si II λ2515 data and the Si IV column density by the Si IV λ1394 data.

There also exist *HST*/FOS spectra of this quasar that covers additional silicon transitions, among other metal lines; however, we

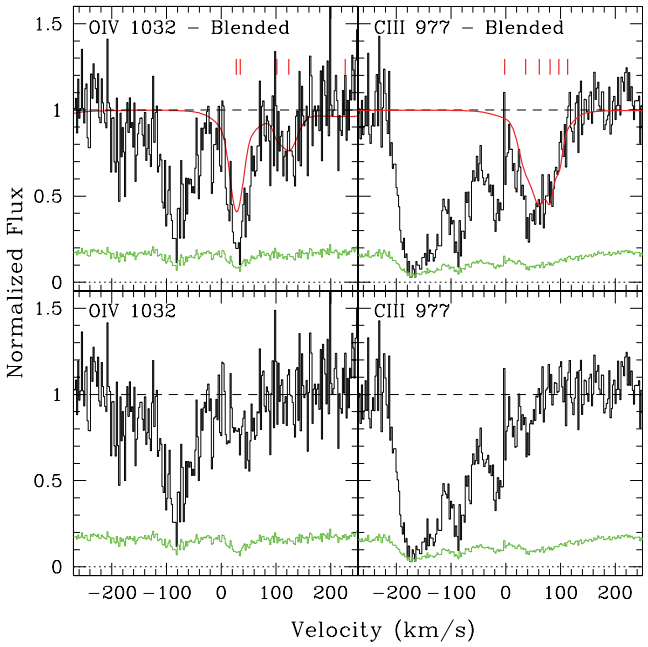


**Figure 3.** Top-left: COS/*HST* O VI λ1032 transition associated with G2 is blended with Ly$\beta$ from the $z = 0.67$ G1 Ly$\alpha$ complex (Churchill et al. 2007, 2012b). The Ly$\beta$ fit (red) was constrained by simultaneous Voigt profile (VP) fits to the Ly$\alpha$, Ly$\gamma$, Ly$\epsilon$ and Ly$\zeta$. Top-right: COS/*HST* C III λ977 transition associated with G2 is blended with Ly$\gamma$ from the $z = 0.67$ G1 Ly$\alpha$ complex (Churchill et al. 2007, 2012b). The VP fit was constrained by the Ly$\alpha$, Ly$\beta$, Ly$\epsilon$ and Ly$\zeta$ which produce the Ly$\gamma$ fit shown (red). Bottom-left: the deblended O VI 1032 line associated with G2. Bottom-right: the deblended C III λ977 line associated with G2.

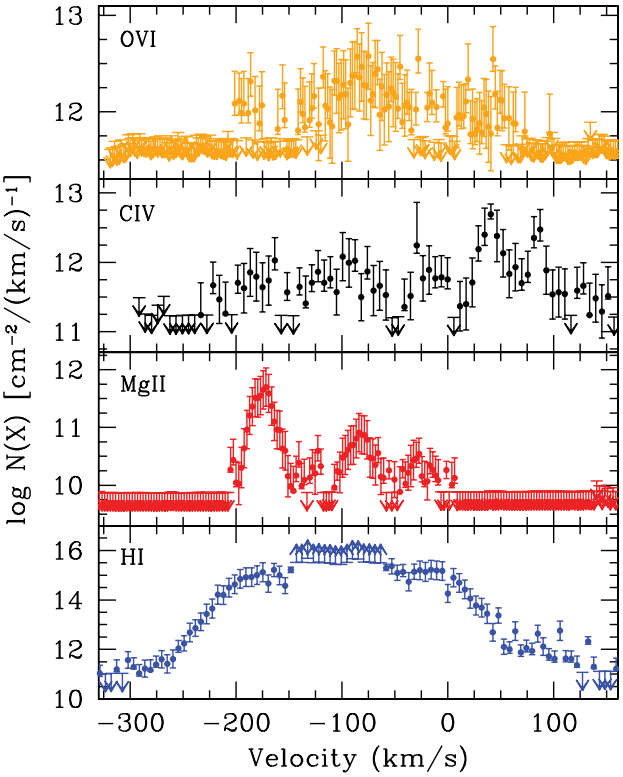


**Figure 4.** The doublet optimally combined AOD distribution for O VI (orange), C IV (black) and Mg II (red). The H I (blue) optical depth distribution was produced by combining the entire Lyman series. The total column densities are integrated over the velocity bins. Note that H I is still saturated in the centre of the profile. Also note the velocity structure difference between the profiles and that the majority of hydrogen is at velocities consistent with Mg II, whereas the majority of C IV has velocities consistent with a small fraction of the total H I.

found that the equivalent widths were inconsistent with the predictions by the COG analysis. This was not the case for the STIS or COS data. We note that the FOS measurements published in Jannuzi et al. (1998) and Churchill et al. (2000) are plagued by unresolved blends from the other H I lines, and therefore we do not use the FOS data in our analysis.

It is important to state that although the COG analysis seems to systematically underestimate the column densities of the metal lines (Prochaska 2006), the silicon transitions do not provide sufficient constraints on our analysis and do not affect our results. We provide these column density measurements for completeness.

## 4 RESULTS: GALAXY PROPERTIES

In Fig. 1 we present a $g'i'Ks$ colour composite centred on the quasar with galaxies G1 and G2 labelled. We find that G2 tends to be bluer than G1, which likely indicates a younger stellar population. This is coincident with the fact that G1 exhibits weak (3 Å) [O II] emission.

In Fig. 5, the $g-r$ versus $i-K$ colours of G1 and G2 are compared to the Bruzual & Charlot (2003) stellar population models obtained using EZGAL (Mancone & Gonzalez 2012) for an exponential star formation history, with an $e$-folding time of 1 Gyr, and a Chabrier (2003) initial mass function. The $K$ band is crucial in breaking degeneracies between other star formation history models since it is very sensitive to the old stellar populations. We tested a variety of models and found that anything but a prolonged $\tau = 1$ Gyr exponential model does not fit the data.

In our companion paper (Churchill et al. 2012b) we discuss G1, although we note that G1 is redder, formed at an earlier epoch and is more massive. The model comparison suggests that G2 is dominated by an ∼4 Gyr stellar population with slightly greater than solar metallicity abundance and formed at redshift $z \sim 2$. We also note that while G2 has an [O II] rest equivalent width of 3.0 Å, it is consistent with galaxies having $U-B \gtrsim 1.0$ (Cooper et al. 2006): red galaxies with little-to-no star formation. Thus, the stellar population of G2 should be dominated by an older population as the model suggests. Adopting the $K$-band mass-to-light ratio associated with this stellar population model, we estimate the total stellar mass of G2 to be $M_* \sim 1 \times 10^{11}$ M$_\odot$.

We further estimate the halo virial mass from the stellar mass using GalMass (Stewart 2011). GalMass uses abundance matching models from Moster et al. (2010) along with semi-empirical fits to observed galaxy gas fractions to convert between the stellar and gas masses described in Stewart et al. (2009). There is roughly a 0.25-dex uncertainty in $M_{\rm vir}$ at a fixed $M_*$ due to the systematics in estimates of $M_*$ (Behroozi, Conroy & Wechsler 2010). The mean galaxy gas and baryonic masses are also estimated from Stewart et al. (2011a) who employed the baryonic Tully–Fisher relation (McGaugh 2005), the relation between stellar, gas and dynamical masses (Erb et al. 2006), and the galaxy gas fraction and stellar mass relation (Stewart et al. 2009). We estimate the halo virial mass, gas mass and baryonic mass to be $\log M_{\rm vir} = 12.9$, $\log M_{\rm gas} = 10.1$ and $\log M_{\rm b} = 11.1$, respectively.

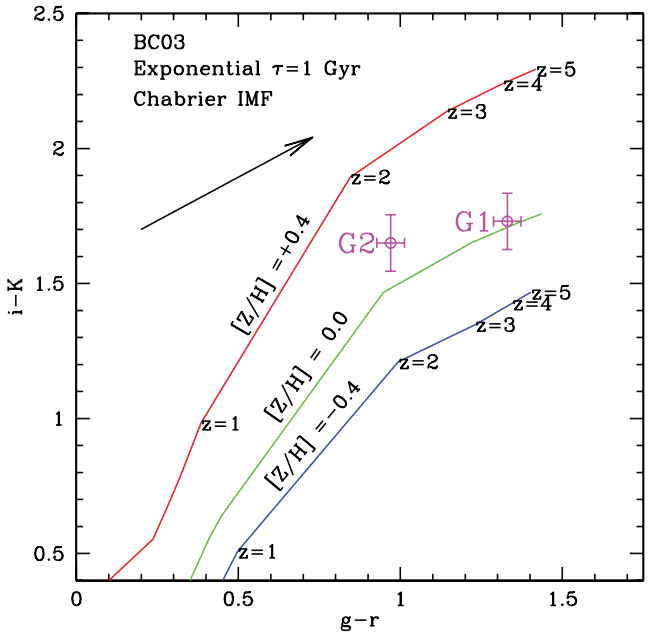


**Figure 5.** Colour–colour diagram for $g-r$ versus $i-K$. The lines denote Bruzual & Charlot (2003) stellar population models for an exponential star formation history and a Chabrier (2003) initial mass function. Stellar metallicities and formation redshifts are also labelled. The points (magenta) represent galaxies G1 and G2, where G2 is the focus of this paper and discussions of G1 can be found in a companion paper (Churchill et al. 2012b). A reddening vector for $E(B-V) = 0.1$ at the rest frame of the galaxies is provided for reference. G2 is consistent with the stellar population model of solar metallicity.

## 5 RESULTS: ABSORPTION

From Figs 2 and 4, it is clear that the absorption properties vary significantly as a function of the ionization level. In Fig. 6, we overlay selected transitions to further demonstrate this. It is clear that Mg II and C III (along with Si II and Mg I) have similar kinematics and trace the bulk of hydrogen. While C IV and O VI trace some of the same gas, their kinematics and their relative absorption strengths differ. Furthermore, they both exist where there are diffuse hydrogen column densities and no Mg II absorption.

In the bottom panels of Fig. 6 we show the AOD column densities as a function of the velocity for each transition. Note that O VI follows similar abundances to C IV across the profile, while Mg II and C III differ and decrease towards the positive velocities. It appears quite clear that the kinematics and the abundance patterns show that C IV and O VI trace different phases of gas, and this difference becomes greater redwards of the galaxy systemic velocity where the hydrogen column density decreases by 2 dex.

Given the observed kinematics and abundance profile differences, we have divided the absorption regions into two separate components and modelled them independently. In Table 1, we list the total column densities for gas bluewards, $N(\mathrm{X})^{\mathrm{blue}}$, and redwards, $N(\mathrm{X})^{\mathrm{red}}$, of the galaxy systemic velocity. In the following subsections, we present models to explain the observed absorption kinematics and also apply photo+collisional ionization models to determine the origins and the physical properties of the gas.

### 5.1 Kinematic models

Steidel et al. (2002) obtained the rotation curve for G2, and it is represented in Fig. 7. Note that all of Mg II, and the majority of

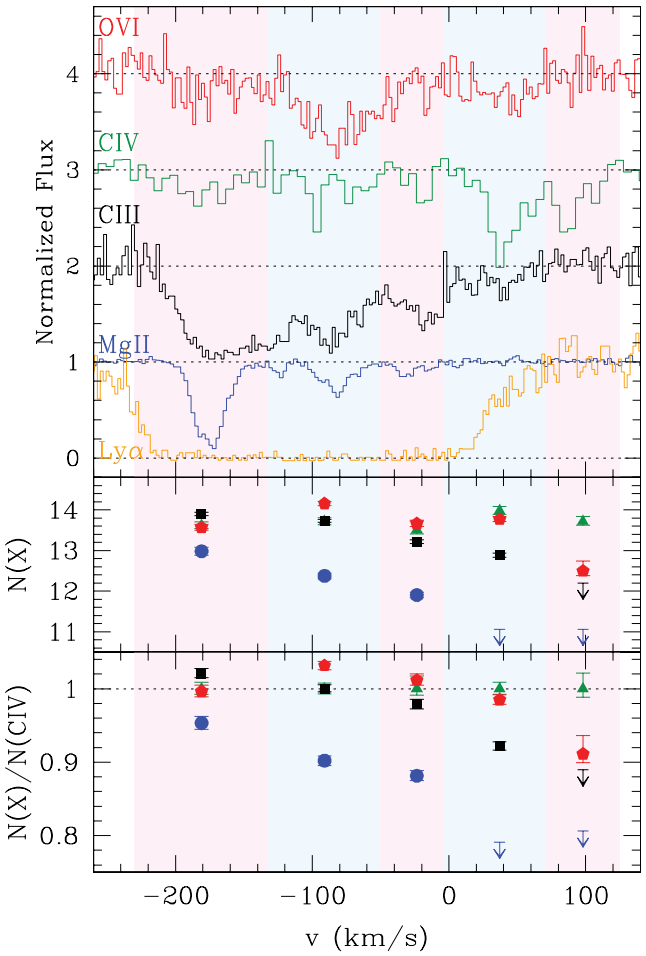


**Figure 6.** Top: an overlay of the Ly$\alpha$, Mg II $\lambda$2796, C III $\lambda$977, C IV $\lambda$1551 and O VI $\lambda$1032 transitions. Note that the low-ionization Mg II $\lambda$2796 and C III $\lambda$977 trace the bulk of hydrogen, while the higher ionization states trace both low and high hydrogen column densities. The line morphologies of C IV and O VI are quite different to those of Mg II and C III. Middle: AOD column densities of Mg II (blue circles), C III (black squares), C IV (green triangles) and O VI (red pentagons) as a function of different velocity bins. The data points are located in the centre of the bin, while the shading indicates the full velocity width of the bin. Bottom: the same as above except that the values are normalized to $N$(C IV). Note that C IV and O VI have similar behaviour bluewards of the systemic velocity.

C III, resides to one side of the galaxy systemic velocity. Churchill & Steidel (2003) noted that C IV, and here we see that O VI, resides on both sides of the galaxy systemic velocity.

To explore the origins of the Mg II absorption, Steidel et al. (2002) employed a simple lagging halo model that extended the galaxy rotation velocity out into a corotating gaseous disc/halo. They determined that a lagging halo model can account for all of Mg II absorbing gas kinematics, even though the absorption occurs at $D = 103.9$ kpc. The predicted model velocities are highlighted by the hashed (blue) region below the galaxy rotation curve in Fig. 7. Further note that the observed rotation curve does not go deep enough to reach the flat part of the curve. This implies that there is additional/higher galaxy kinematics that was not included in the model; thus, the vertical solid (blue) line on the left of the absorption profiles would move towards bluer velocities. It is quite clear that the low-ionization gas seems to be coupled to the disc kinematics similar to the models of Stewart et al. (2011b). However, the observed

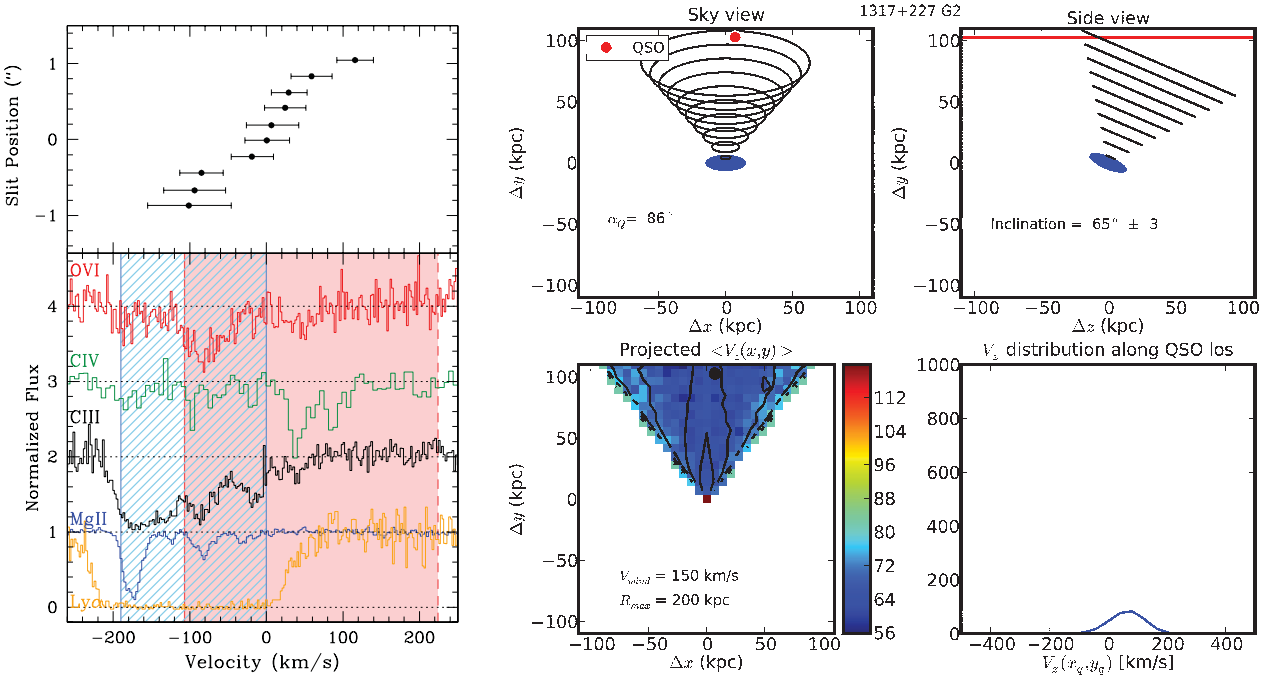


**Figure 7.** Left: the data points show the rotation curve of G2 obtained from Steidel et al. (2002). Below is a selection of absorption transitions where the hashed region (blue) shows the rotating thick disc modelled velocities, while the solid shading (red) indicates the wind model velocity predictions. Note that all of Mg II, and the majority of C III, resides to one side of the galaxy systemic velocity, while C IV, and some O VI and C III also reside redwards of the galaxy systemic velocity. Right: the wind model of Bouché et al. (2012) applied to G2. Top-left panel: the wind modelled cone, having an opening angle of 30°, viewed face-on where the galaxy is represented as the filled ellipse and with the QSO line of sight marked. Top-right panel: a side view. Bottom-left panel: the average cloud line-of-sight velocities as a function of the position within the wind. The QSO location is represented as the filled circle. Bottom-right panel: the line-of-sight velocity distribution of the clouds at the location of the quasar. We find that an outflow velocity of 150 km s$^{-1}$ produces a good match to the data and is comparable to the results found by Bouché et al. (2012). Note that the peak of the density distribution coincides with the bulk of the C IV absorption.

corotating Mg II absorption extends to larger $D$ than the models of Stewart et al. (2011b) since at $z = 1.4$ their simulated discs extend only to ∼40 kpc. Thus, it remains unclear if there is size evolution as a function of redshift or if the simulations (without metals) properly trace the metal lines or if this is a result of simulating only a few galaxies. Aside from these caveats, the similarities between the observations and the simulations suggest that this absorption system exhibits signatures of cold-mode accretion.

Note that the rotating disc model does not account for all of the absorption. Perhaps given that the quasar line of sight passes along the minor axis of the galaxy and that G2 is undergoing some star formation (indicated by the [O II] emission shown in Fig. 1), it is possible that some of the absorption arises from outflows.

By analysing 10 $z \sim 0.1$ Mg II absorbers selected from Kacprzak et al. (2011a), Bouché et al. (2012) found a bimodal distribution of the azimuthal orientation of the quasar sightlines: half of the sightlines aligned with the major axis and half within $\alpha = 30°$ of the minor axis. The bimodal azimuthal angle distribution was later confirmed by Kacprzak et al. (2012) using a sample of 88 absorption-selected galaxies ($W_r(2796) \geq 0.1$ Å) and 35 non-absorbing galaxies ($W_r(2796) < 0.1$ Å). These results indicate that both gaseous discs and strong bipolar outflows could contribute to Mg II cross-section. Bouché et al. (2012) also applied a simple biconical wind model that was able to reproduce the observed Mg II kinematics for the sightlines aligned with the minor axis. We apply their model here in an effort to reproduce the observed absorption kinematics. Their galactic wind model consists of $10^5$ 'clouds' moving at a constant velocity ($V_{out}$) that is determined from the absorption data. The clouds are contained within a cone that has a 30° opening angle.

Fig. 7 shows the wind model for G2 using the orientation parameters from Kacprzak et al. (2011b). The top-left panel shows the cone view face-on and the top-right panel shows a side view of the cone, where the galaxy is represented as the filled ellipse and with the QSO line of sight marked. The bottom-left panel shows the average cloud line-of-sight velocities as a function of the position. The bottom-right panel shows the distribution of the cloud line-of-sight velocities along the quasar sightline. The wind speed is tuned to match the observed velocity range. For this particular case, we find that an outflow velocity of 150 km s$^{-1}$ produces a good match to the data and they are comparable to the results found by Bouché et al. (2012).

In the lower-right panel, we see that the predicted absorption distribution peaks at roughly 50 km s$^{-1}$, where the majority of C IV and some O VI reside. The wind model velocity range is also shown as the solid shaded region over the absorption profiles. The model could also account for the observed C IV and O VI bluewards of the galaxy systemic velocity, although the model predicts only that a few percent of the gas is expected at these velocities.

If the opening angle or the wind speed is increased, the model velocity range would also increase and could include all of the observed absorption. However, increasing these parameters will not reproduce the observed optical depth distribution of the cold and hot gas. While our current model is tuned to reproduce the absorption redwards of the galaxy systemic velocity, a different model would not be able to predict the strong absorption residing at −200 km s$^{-1}$. A model with increased opening angle and/or wind speed would also predict additional absorption beyond +200 km s$^{-1}$ where none is observed. Therefore, it is very difficult to reproduce both the velocity

and optical depth distributions of the cold and hot gas using only the wind model.

The wind model cannot account for the bulk of Mg II, Mg I, Si II and C III. Thus, although the galaxy is forming stars, winds are likely not responsible for the cool gas, but could be responsible for the hot gas. One would naively expect that the infalling gas would be metal poor while the outflowing gas be metal enriched. We explore the gas-phase metallicities in the next subsections in order to determine the possible origins of the absorption.

### 5.2 Cold gas phase

To determine the physical properties of the cool gas bluewards of the galaxy systemic velocity, we use CLOUDY (Ferland et al. 1998) to model the ionization conditions. We follow the standard assumption of a photoionized uniform slab of gas that is in ionization equilibrium and is illuminated with a Haardt & Madau (2012) ionizing spectrum, where the ultraviolet (UV) photons arise from quasars and galaxies. The ionization parameters, $U$, and the metallicity of the gas are varied to match the observations of $N(\mathrm{X})^{\mathrm{blue}}$ in Table 1 (column 6).

In Fig. 8 we show the model results computed for $\log[N(\mathrm{H\,I})] = 18.3 \pm 0.3$ and a metallicity of $[\mathrm{X/H}] = -1.67$. We find a narrow range of ionization parameters that reproduce the cool gas phase. The thin curves show the models while the thicker curves show the model values permitted by the data. C III provides the tightest constraints on the ionization parameter of $-3.44 \leq \log U \leq -3.00$.

In Fig. 8, the same CLOUDY models are shown as a function of $U$ and metallicity. The constraints placed on $U$ and the models confine the allowed range of metallicity. The C III measurements limit the metallicity to $-2.06 \leq [\mathrm{X/H}] \leq -1.32$. Recall that the C III column density measurement bluewards of the galaxy systemic velocity is the unblended portion of this transition. If we were to include the small contribution of C III redwards of the galaxy systemic velocity, our results would still be consistent. Thus, this cool gas component has low metallicity and a low-ionization parameter.

In summary, the C III column density provides the tightest constraint and yields $\log U = -3.22 \pm 0.22$ and $[\mathrm{X/H}] = -1.69 \pm 0.37$. The gas is primarily ionized since the ionization fraction $X(\mathrm{H\,I}) = N(\mathrm{H\,I})/N(\mathrm{H}) = 0.05 \pm 0.02$ with a hydrogen number density of $\log(n_{\mathrm{H}}) = -1.86 \pm 0.22$.

Note that C IV and O VI do not appear on these plots. The column densities predicted for this photoionized modelled gas would be $\log N(\mathrm{C\,IV}) = 11.88$–$11.94$ and $\log N(\mathrm{O\,VI}) = 7.29$–$7.35$. These predicted column densities are nowhere near the measured values of $\log N(\mathrm{C\,IV}) = 14.11$ and $\log N(\mathrm{O\,VI}) = 14.33$. Thus, it is likely that these ions are not part of the cool gas phase and are likely part of a separate 'warm/hot' collisional ionized gas phase. In Fig. 6, note that C IV and O VI have different kinematics and that the lower ionization species further indicated that the absorption bluewards of the galaxy systemic velocity is probing two gas phases. In the next section we model the warm gas.

### 5.3 Warm gas phase

We employed our own photo+collisional ionization code (Churchill & Klimek, in preparation) to model the warm gas phase since it is

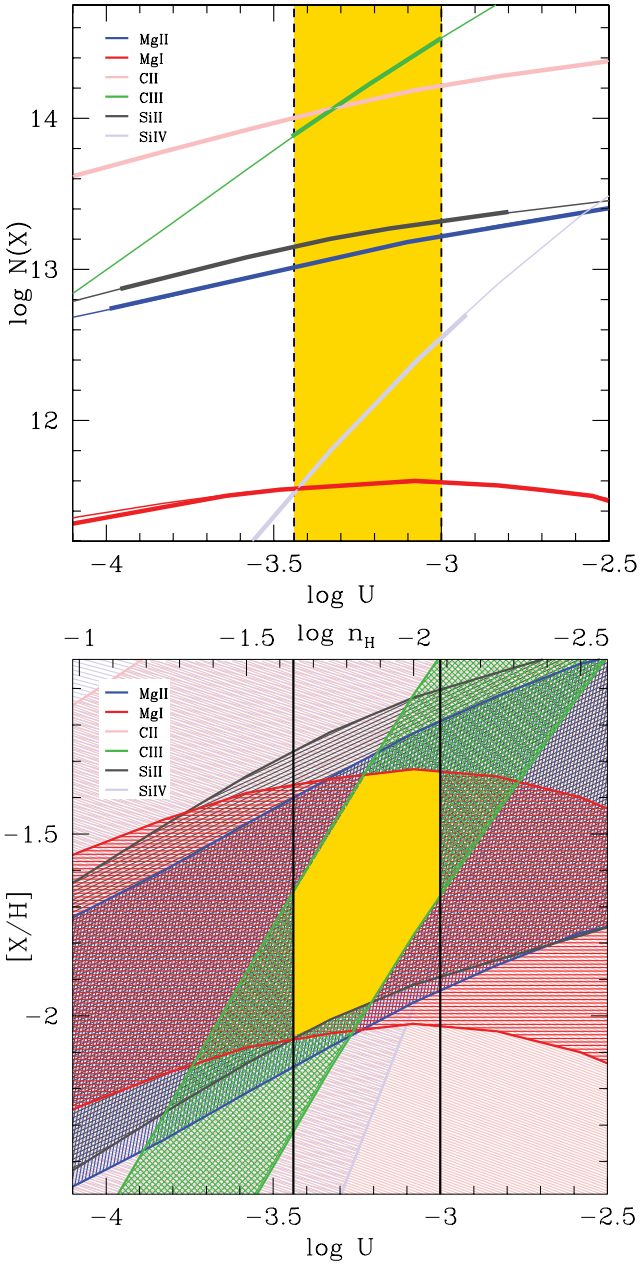


**Figure 8.** Top: the CLOUDY predicted column densities, as a function of the ionization parameter, for a metallicity of $[\mathrm{X/H}] = -1.67$ and $\log[N(\mathrm{H\,I})] = 18.3 \pm 0.3$. The bold portions of the curves show the observed column densities, $N(\mathrm{X})^{\mathrm{blue}}$, bluewards of the galaxy systemic velocity (Table 1, column 6). The vertical lines show the ionization parameter constraints provided by the data. C III provides the tightest constraints of $-3.44 \leq \log U \leq -3.00$ indicated between the solid vertical lines (gold region). Si II and Mg II provide secondary constraints of $-3.38 \leq \log U \leq -3.16$ as indicated by the vertical dashed lines (yellow region). Bottom: the ionization parameter as a function of metallicity for the above model. The shaded regions show the model ranges due to the measurement errors in $N(\mathrm{X})^{\mathrm{blue}}$. The vertical lines represent the ionization parameter constraints provided by the top panel and provide the region of acceptable metallicities. The overlapping shaded regions of each ion within the constraints provided by $U$ have solid shading and outline the allowed metallicities of this cold gas. Again, C III places the tightest constraints on the metallicity $-2.06 \leq [\mathrm{X/H}] \leq -1.32$. Thus, the cool gas has low metallicity and a low-ionization parameter.

optimally designed for optically thin gas with no ionization structure. In short, the code incorporates photoionization, Auger ionization, direct collisional ionization, excitation–autoionization, photorecombination, high/low temperature dielectronic recombination, charge transfer ionization by $H^+$, and charge transfer recombination by $H^0$ and $He^0$. All metal transitions and ionization stages for elements up to zinc are modelled. Solar abundance mass fractions are obtained from Draine (2011) and Asplund et al. (2009), and a Haardt & Madau (2012) ionizing spectrum is used for the UV background. The model inputs are the hydrogen number density ($n_{\rm H}$), the kinetic temperature and the gas metallicity, while the model outputs are the electron density, the ionization and recombination rate coefficients, the ionization fractions and the number densities for all ionic species. Our models are consistent with those of CLOUDY for $\log(n_{\rm H}) > -3.75$. For $\log(n_{\rm H}) < -3.75$, cosmic ray heating in CLOUDY tends to yield overionized clouds with large sizes (<100 kpc). When cosmic ray heating is turned off, CLOUDY has convergence issues and tends to produce ratios of column densities for adjacent species that do not follow a trend physical with ionization potential. We have reconciled these issues in our models, and a detailed comparison will be presented in Churchill & Klimek (in preparation).

### 5.3.1 *Warm gas phase bluewards of the systemic velocity*

In modelling the cold gas phase we noted that we are unable to account for the measured $\log N(\text{C IV}) = 14.11$ and $\log N(\text{O VI}) = 14.33$. Thus, these ions are not part of the cool gas phase and are likely part of a separate warm collisionally ionized gas phase. Here we model the diffuse warm gas found bluewards of G2's systemic velocity. Furthermore, all of the measured C III is well modelled as being associated with the cool gas phase; however, there could possibly exist a small fraction of a measurable warm C III component hidden. If we assume that the warm component is within the 0.2-dex measurement error of C III, then there can be at most $\log N(\text{C III}) < 12.87$ in the warm phase.

In Fig. 9 we show column density ratios, which are independent of $N$(H I), as a function of temperature and hydrogen density. The solid line denotes the C IV/O VI column density ratio along with its measured error (dotted lines). The long and short dashed lines represent the C III/C IV and C III/O VI column density ratios, respectively. The dashed curves denote lower limits on the allowed temperature range for a given hydrogen density since $\log N(\text{C III}) < 12.87$. Note that full self-consistency is achieved when the dashed curves fall below the solid curve. The models indicated that the gas has a hydrogen density of $\log n_{\rm H} > -3.5$ and C IV/O VI provides temperature constraints of $\log T = 5.23-5.29$, where the exact temperature is dependent on $n_{\rm H}$.

In Fig. 9, we also show the gas metallicity as a function of $N$(H I) and $n_{\rm H}$. We are unable to measure the H I column density associated with this warm component. However, Churchill et al. (2007) state that if an additional hydrogen component having $\log N(\text{H I}) > 16.8$ were added to the total hydrogen column density, then it would measurably modify the shape of the Lyman limit. Thus, this provides a conservative estimate of the additional $N$(H I) that could be associated with the warm component since we assume that it cannot contribute to the Lyman limit. The column density limits provide a metallicity limit of $[\text{X/H}] \lesssim -0.5$. Note that the metallicity scales with the hydrogen column density by the same amount. It is likely that the metallicity is much lower, though we cannot provide any further constraints.

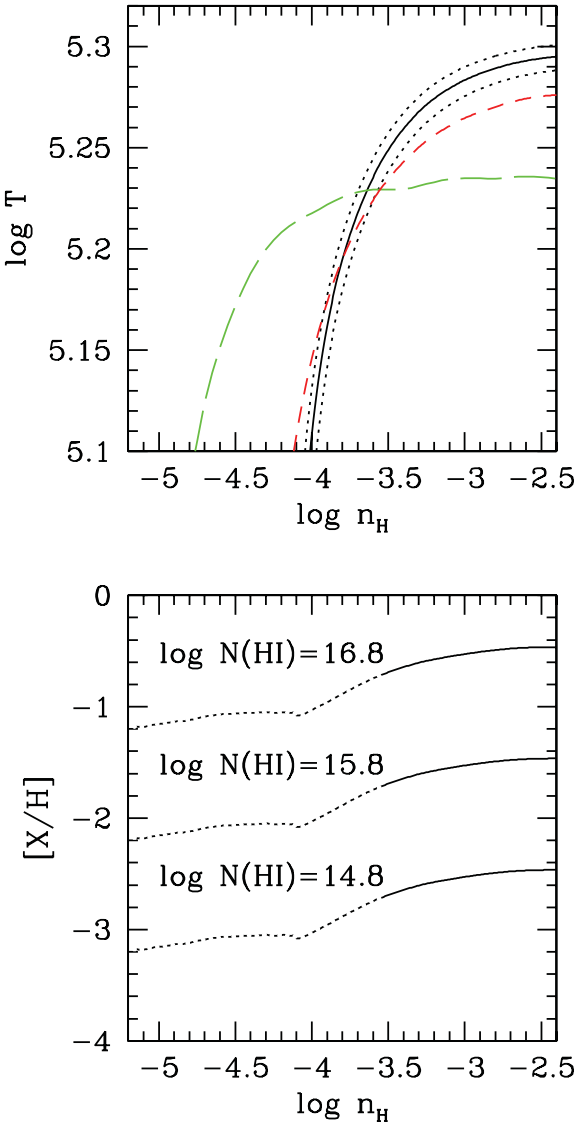


**Figure 9.** Top: the photo+collisional ionization models (Churchill & Klimek, in preparation) as a function of temperature and hydrogen density. The lines indicate abundance ratios which are independent of the hydrogen column density. The solid line denotes the C IV/O VI column density ratio along with its measured error (dotted lines). The long and short dashed lines represent the C III/C IV and C III/O VI column density ratios, respectively. The C III/C IV and C III/O VI dashed curves denote lower limits on the allowed temperature range for a given hydrogen density. Note that full self-consistency is achieved when the dashed curves fall below the black curve. The gas has a hydrogen density of $\log n_{\rm H} > -3.5$, and C IV/O VI provides a temperature constraint of $\log T = 5.23-5.29$. Bottom: the metallicity as a function of the hydrogen density for various hydrogen column densities. We provide a conservative limit of $\log N(\text{H I}) < 16.8$ (see the text) which yields $[\text{X/H}] < -0.5$.

### 5.3.2 *Warm gas phase redwards of the systemic velocity*

Here we model the diffuse warm gas found redwards of G2's systemic velocity. We allowed the gas temperature, the gas metallicity and the hydrogen density to vary to match the column density measurements, $N(\text{X})^{\rm red}$, from Table 1 (column 8). We only detect C III, C IV and O VI redwards of the galaxy systemic velocity. H I associated with the warm gas phase was computed from the AOD H I column density redwards of the galaxy systemic velocity. As shown

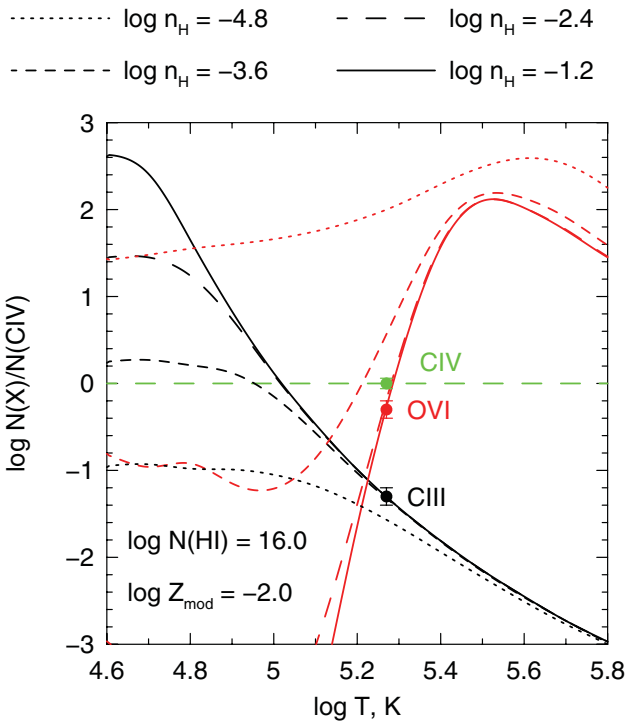


**Figure 10.** The photo+collisional ionization models obtained from Churchill & Klimek (in preparation) as a function of the temperature and column density normalized to $N$(C IV). The data points are the AOD measured column densities of absorption redwards of G2's systemic velocity, $N(\mathrm{X})^{\mathrm{red}}$, shown in Table 1 (column 8). We allowed the gas temperature and metallicity to vary for a range of hydrogen densities, $n_{\mathrm{H}}$. The data constrain the gas temperature to be 185 000 K and limit $\log n_{\mathrm{H}} \geq -2.4$. In Fig. 11 we provide the constraints on the warm-phase metallicity.

in Fig. 4, the H I absorption profile is not saturated redwards of the galaxy systemic velocity and contains $\log N(\mathrm{H\,I}) = 16.03 \pm 0.18$.

Fig. 10 shows the models' column densities normalized to that of C IV. The data are well constrained with the warm gas phase having a temperature of $T = 185\,000$ K, while there seems to be a larger range in the hydrogen density such that $\log n_{\mathrm{H}} \geq -2.4$ for a fixed metallicity. In order to accurately determine the range of metallicities and $n_{\mathrm{H}}$, we show the predicted column densities and metallicities as a function of $n_{\mathrm{H}}$ in Fig. 11. Again, the measured (left) and modelled (middle) column densities are shown. The model spread, indicated by the dotted lines, is dominated by the error in the measured H I column density. We find that the models do not well constrain $n_{\mathrm{H}}$ but provide reasonable constraints on the metallicity. We find $-2.50 \leq [\mathrm{X/H}] \leq -1.93$ and $\log n_{\mathrm{H}} > -3.3$ for the lower metallicity limit and $\log n_{\mathrm{H}} > -2.1$ for the upper metallicity limit.

## 6 DISCUSSION

The galaxy G2 has a stellar metallicity greater than solar, yet it contains the [X/H] $\sim -2$ halo gas detected in absorption at 104 kpc from the galaxy centre. The data likely suggest that the absorbing gas is tracing cold accretion. A summary of the absorption gas properties is presented in Table 2. The kinematic differences[4] seen between the high- and low-ionization states, as shown in Fig. 6, and the photo+collisional ionization models suggest that the absorption is multiphase. This may imply that the warm and cold gas physically arise in different locations or that the absorbing gas is not well mixed.

The quasar sightline probes absorption within 3° of the projected minor axis of G2 (Kacprzak et al. 2011b), which is a location recently interpreted to be favourable for probing galactic-scale winds (Bordoloi et al. 2012; Bouché et al. 2012; Kacprzak et al. 2012). G2 is dominated by a relatively old stellar population, yet it has measurable [O II] emission (3.0 Å) and thus is likely undergoing some current star formation that could possibly produce winds.

In Fig. 7 we show a wind model that can account for the bulk of the warm gas kinematics, both redwards and bluewards of G2's systemic velocity, yet it does not reproduce the kinematics of the cold gas. This might imply that some of the warm gas could originate from winds; however, the 2–2.5 order of magnitude difference between the galaxy stellar metallicity and the absorption metallicity is inconsistent with a wind model (e.g. Oppenheimer et al. 2010). Assuming a constant wind speed of 150 km s$^{-1}$, as suggested by the models, the absorbing gas would have left the galaxy 670 Myr ago. Given such a short time-scale, G2 is still expected to have solar metallicity at that epoch according to mass–gas metallicity relations (e.g. Savaglio et al. 2005) and simulations (e.g. Oppenheimer et al. 2010). The recycling for wind material is less than 1 Gyr (Oppenheimer et al. 2010); thus, if the gas were wind material and well mixed, then it would be expected to have a metallicity similar to that of the parent stellar population. However, the efficiency at which the gas is mixed within the halo environment is still unclear. Sijacki et al. (2012) show that poor gas mixing in simulations may be an artefact of the suppression of dynamical fluid instabilities demonstrated by comparing smoothed particle hydrodynamics (SPH) codes to that of the moving mesh code AREPO. However, some LLSs exhibit metallicity variations across the absorption profile (e.g. Prochter et al. 2010). Thus, if the gas probed by this absorption system is poorly mixed, it is plausible that the gas is entrained in an outflowing wind (see Schaye, Carswell & Kim 2007; Alūzas et al. 2012). However, the current observational evidence suggests that Mg II entrained in outflowing material may, on average, have a maximum projected extension of ∼50 kpc. (Bordoloi et al. 2012). Thus, the combination of low metallicity, the relative kinematics between the galaxy and the absorbing gas, and the large projected distance between the gas and the galaxy corroborates an accretion scenario.

In summary, although the kinematic model works well for the warm gas, it is inconsistent with the expected outflow metallicities, and this gas would have already been recycled several times and should have nearly solar metallicity. This leads to the idea that this meal-poor gas could be infalling towards the galaxy.

Galaxy G2 has a stellar mass of $M_* = 1 \times 10^{11}$ M$_\odot$ and a virial mass of $M_{\mathrm{vir}} = 8 \times 10^{12}$ M$_\odot$. Cold-mode accretion is less favoured for galaxies with $M_{\mathrm{vir}} \gtrsim 10^{12}$ M$_\odot$ since the cold gas can become shock-heated as it enters the halo and hot-mode accretion becomes the dominant mode of accretion (e.g. Dekel & Birnboim 2006; Kereš et al. 2009; Stewart et al. 2011a,b; van de Voort & Schaye 2011; van de Voort et al. 2011). For massive galaxies, infalling gas can be shock-heated to temperatures above $10^6$ K; however, accretion via dense filaments can be maintained past the shock regions, although having dramatically decreased covering fractions compared to low-mass galaxies, and still accreting on to the galaxy (e.g. Kereš et al. 2009; Faucher-Giguère et al. 2011; Stewart et al. 2011a,b; van de Voort & Schaye 2011; van de Voort et al. 2011). The hot gas pressure compresses cold streams and provides an efficient means of bringing cold pristine gas to the host galaxy and should

[4] Ding et al. (2005) modelled the C IV and lower ionization states of Mg II, Mg I and Fe II with the same kinematic structure. It is clear from the fit residuals that the kinematics are not well modelled with similar velocity structure although they do have some similarities.

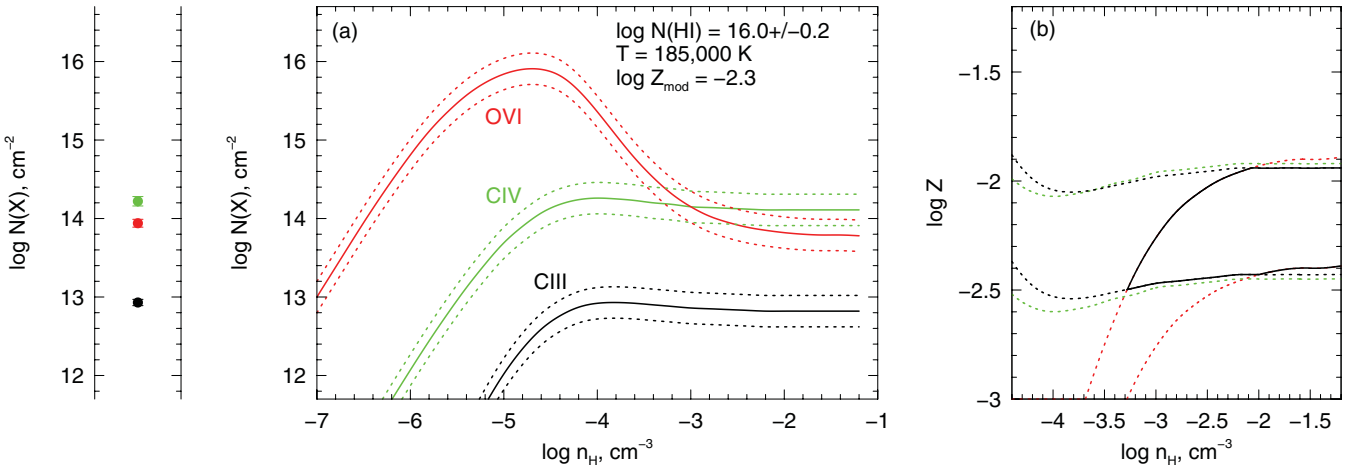


**Figure 11.** Left: the data points are the AOD measured column densities of absorption redwards of G2's systemic velocity, $N(\mathrm{X})^{\mathrm{red}}$, shown in Table 1 (column 8). Middle: the photo+collisional ionization models obtained from Churchill & Klimek (in preparation) for C III, C IV and O VI using a fixed temperature of 185 000 K and [X/H] = −2.3. The spread in the models is due to the error in the measured H I column density of $\log[N(\mathrm{H\,I})] = 16.03 \pm 0.18$ (dotted lines). Right: the allowed metallicity and $n_{\mathrm{H}}$ for the model on the left. While $n_{\mathrm{H}}$ is not well constrained, we find $-2.50 \leq [\mathrm{X/H}] \leq -1.93$ and $\log n_{\mathrm{H}} > -3.3$ for the lower metallicity limit and $\log n_{\mathrm{H}} > -2.1$ for the upper metallicity limit.

**Table 2.** Modelled absorbing gas properties.

| Name | Velocity (km s$^{-1}$) | log $N$(H I) | log($T$) | log($U$) | log($n_{\mathrm{H}}$) | [X/H] |
|---|---|---|---|---|---|---|
| Cold | $-240 \leq v_{\mathrm{abs}} \leq -3$ | $18.3 \pm 0.3$ | 3.82−5.23 | $-3.44 \leq \log(U) \leq -3.00$ | $-2.08 \leq \log(n_{\mathrm{H}}) \leq -1.64$ | $-2.06 \leq [\mathrm{X/H}] \leq -1.32$ |
| Warm blue | $-240 \leq v_{\mathrm{abs}} \leq -3$ | $<16.8^a$ | 5.23−5.29 | $\log(U) \geq -3.5$ | $\log(n_{\mathrm{H}}) > -3.5$ | $[\mathrm{X/H}] \leq -0.5^a$ |
| Warm red | $-3 \leq v_{\mathrm{abs}} \leq 220$ | $16.0 \pm 0.18$ | 5.27 | $\log(U) \geq -3.3$ | $\log(n_{\mathrm{H}}) > -3.3$ | $-2.50 \leq [\mathrm{X/H}] \leq -1.93$ |

[a]See the text in Section 5.3.1 for a discussion of the $N$(H I) upper limit used and how this affects the absorption metallicity.

be traced by LLS (e.g. Fumagalli et al. 2011). $\log N(\mathrm{H\,I}) = 18.3$ corresponds to $\Delta\rho/\rho > 1000$ at $z \leq 1$ (e.g. Davé et al. 1999) indicating that these high densities could make their way into the galaxy centre.

Although massive galaxy haloes are built up from hot accretion, comprising 80–90 per cent of the total accretion, accretion on to the interstellar medium (ISM) becomes less important (50–70 per cent hot mode (van de Voort et al. 2011). However, van de Voort et al. (2011) state that the cold gas accreting on to the ISM in massive galaxies increases with increasing simulation resolution. This could arise since gas clouds could be easily disrupted in SPH simulations, and the cold fraction would increase if higher densities were reached in higher resolution simulations. A lower hot fraction of gas accreting on to the galaxy occurs because the hot gas temperature increases with the virial temperature, or the halo mass, resulting in longer cooling times (e.g. Wiersma, Schaye & Smith 2009) and yielding less hot gas cooling to ISM temperatures. However, these results could also be dependent on the type of simulations used (Sijacki et al. 2012).

Using the cosmological formulae for virial quantities of Bryan & Norman (1998), we derived the radius $R_{\mathrm{vir}} = 380$ kpc, the circular velocity $v_{\mathrm{circ}} = 280$ km s$^{-1}$ and the temperature $T_{\mathrm{vir}} = 3 \times 10^6$ K. The quasar is probing along the minor axis of the galaxy within the virial radius at $R/R_{\mathrm{vir}} \sim 0.3$, well within the shock radius. Furthermore, the halo gas is expected to be heated to the virial temperature. The temperatures deduced from our models for the warm gas phase are $1.8 \times 10^5$ K for the gas bluewards of the systemic velocity and $1.9 \times 10^5$ K for the gas redwards of the galaxy systemic velocity; both are an order of magnitude cooler than the virial temperature. However, this gas can possibly cool after it had been shocked, although as mentioned above, the cooling time for hot shock-heated gas is much longer for massive galaxies.

We can estimate a cool gas-phase temperature by using the Doppler parameters derived from Mg II absorption (Kacprzak et al. 2011b). The Mg II Doppler parameters range from 2.1 to 10.8 km s$^{-1}$, and if we assume that all the broadening is thermal, we can compute upper limits on the temperature of $6.6 \times 10^3 - 1.7 \times 10^5$ K. These temperatures are upper limits since some of the line-broadening could be due to turbulence, and the VP fits to the data assume a minimum number of 'clouds'; if more clouds were inserted, then the velocity width of each line would decrease. Thus, the cold gas has temperatures well expected for cold-mode accretion and not post-shock-heated cooling gas accreting within a virial radius ratio of 0.3 (van de Voort & Schaye 2011).

The absorption kinematics also hints to an origin of cold-mode accretion. The metal-poor cold phase, and the redward warm phase, has kinematics consistent with extended disc rotation (Steidel et al. 2002; Kacprzak et al. 2010a). This result has been interpreted using cosmological simulations to be a signature of cold gas accreting via filaments that drive the angular moment of the galaxy, thereby mimicking its rotation out at larger impact parameters (Kacprzak et al. 2010a; Stewart et al. 2011b). This is consistent with van de Voort & Schaye (2011) that shows cold accretion gas having higher radial velocities that scale with the increase in mass compared to the flat radial velocity distribution of the hot-mode accretion as a function of mass.

As we previously mentioned, the metallicities of the warm ([X/H] = −2 to −2.5) and cold ([X/H] = −1.7) gas are low and appear to be consistent with metallicities expected for cold-mode accretion at $R/R_{\mathrm{vir}} \sim 0.3$ (van de Voort & Schaye 2011) and do

not mimic the metallicities expected for the ISM, the hot halo and the host galaxy (Oppenheimer et al. 2010). The temperatures and kinematics of the absorbing gas are also consistent with what is expected for cold-mode accretion. Thus, it is likely that the absorption is probing cold pristine gas infalling towards the centre of the disc, further fuelling star formation.

## 7 CONCLUSIONS

In this paper, we present detailed photo+collisional ionization models and kinematic models of the multiphase absorbing gas, detected within the *HST*/COS, *HST*/STIS and Keck/HIRES spectra of the background quasar TON 153, associated with a star-forming spiral galaxy at $z = 0.6610$. The sightline probes the projected minor axis of the galaxy at a projected distance of 0.3 virial radii, well inside the virial shock radius predicted for a galaxy of this mass, implying that if the gas is infalling, then it is post-shock-heated accretion or a cold filament. We obtained follow-up *HST*/COS data to study other metal lines in order to determine the halo gas properties and their origins. This galaxy was targeted as a candidate cold accretion probe supported by kinematics and orientation results presented by Steidel et al. (2002) and Kacprzak et al. (2010a, 2011b).

Our main results can be summarized as follows.

(i) From $g'r'i'Ks$ photometry and stellar population models, we determined that G2 is dominated by an $\sim$4 Gyr stellar population with slightly greater than solar metallicity abundance and is formed at redshift $z \sim 2$. We estimate $M_* = 1 \times 10^{11}$ M$_\odot$ implying $\log M_{\rm vir} = 12.9$.

(ii) The low-ionization states, Mg I, Si II, Mg II and C III, have similar absorption kinematics, abundance ratios across the profile, and trace the bulk of hydrogen, while C IV and O VI trace some of the same gas, their kinematics, abundance ratios and their relative absorption strengths differ. We infer that the low- and high-ionization states trace different gas phases.

(iii) Modelling the cold gas bluewards of G2's systemic velocity, $N(\rm X)^{blue}$, we constrain $\log T = 3.82{-}5.23$, $-3.44 \leq \log(U) \leq -3.00$, $-2.08 \leq \log(n_{\rm H}) \leq -1.64$ and $-2.06 \leq$ [X/H] $\leq -1.32$. The gas is cold and very metal poor, consistent with cold accretion. We are unable to account for the measured $N$(C IV) and $N$(O VI) when modelling the cold phase; thus, these ions are likely part of a separate warm collisionally ionized gas phase.

(iv) A lagging halo model can account for all of low-ionization absorption, hinting that this gas is coupled to the disc and simulations interpret this as a detection cold-mode accretion.

(v) Modelling the warm gas bluewards of G2's systemic velocity, $N(\rm X)^{blue}$, we find $n_{\rm H} > -3.5$ and $\log T = 5.23$–$5.29$. Armed with only a conservative limit of the hydrogen column density that could be associated with the warm component [$N$(H I) $> 16.8$], we estimate [X/H] $\lesssim -0.5$, although it is highly likely that the metallicity is much lower.

(vi) Modelling the warm gas redwards of G2's systemic velocity, $N(\rm X)^{red}$, we find hot and metal-poor gas with $T = 185\,000$ K, $-2.50 \leq$ [X/H] $\leq -1.93$ and $n_{\rm H} > -3.3$.

(vii) The quasar line of sight passes along G2's minor axis, and a wind model can account for the observed C IV and O VI redwards and bluewards of the galaxy systemic velocity. However, given the 2–2.5 orders of magnitude difference between the galaxy stellar metallicity and the absorption metallicity we demonstrate that the gas cannot arise from galactic winds.

It remains plausible that this low-metallicity gas arises from unidentified satellite around the host galaxy or from the incomplete mixing between metal-enriched and metal-poor halo gas. However, the combination of the relative kinematics, temperatures and relative metallicities allows us to conclude that the multiphase gas detected in absorption likely arises from cold accretion around this massive galaxy. For high-mass galaxies, the cold accretion cross-section is expected to be a few per cent, so our absorption system and others cited in the literature could be a by-chance low-probability intersection of a filament, or the resolution effects in the simulations (see van de Voort & Schaye 2011) are underestimating the covering fraction of cold flows. This system also contradicts current results that predict that all absorption detected in quasars probing gas along the projected minor axis of galaxies is produced by winds (Bordoloi et al. 2012; Bouché et al. 2012; Kacprzak et al. 2012). This is clearly not the case here.

## ACKNOWLEDGMENTS

We thank Nicolas Bouché for his useful comments, models and for carefully reading this paper. We also thank the anonymous referee for carefully reading the paper and for providing insightful comments. CWC was partially supported through grant HST-GO-11667.01-A provided by NASA via the Space Telescope Science Institute, which is operated by the Association of Universities for Research in Astronomy, Inc., under NASA contract NAS 5-26555. CWC thanks GGK, and Michael T. Murphy, and Swinburne Faculty Research Grants for providing funding for a visit to Swinburne University of Technology. This work is based on observations made with the NASA/ESA *Hubble Space Telescope* (PID 11667) and those obtained from the Hubble Legacy Archive, which is a collaboration between the Space Telescope Science Institute (STScI/NASA), the Space Telescope European Coordinating Facility (ST-ECF/ESA) and the Canadian Astronomy Data Centre (CADC/NRC/CSA). Some of the data presented herein were obtained at the W. M. Keck Observatory, which is operated as a scientific partnership among the California Institute of Technology, the University of California and the National Aeronautics and Space Administration. The Observatory was made possible by the generous financial support of the W. M. Keck Foundation. This work is also based on observations obtained with the Apache Point Observatory 3.5-m telescope, which is owned and operated by the Astrophysical Research Consortium. Observations were also made with the NASA/ESA *Hubble Space Telescope* or obtained from the data archive at the Space Telescope Institute.

## REFERENCES

Alūzas R., Pittard J. M., Hartquist T. W., Falle S. A. E. G., Langton R., 2012, MNRAS, 425, 2212
Asplund M., Grevesse N., Sauval A. J., Scott P., 2009, ARA&A, 47, 481
Bahcall J. N. et al., 1993, ApJS, 87, 1
Bahcall J. N. et al., 1996, ApJ, 457, 19
Barlow R., 2003, preprint (arXiv:physics/0306138)
Behroozi P. S., Conroy C., Wechsler R. H., 2010, ApJ, 717, 379
Bertin E., Arnouts S., 1996, A&AS, 117, 393
Bordoloi R. et al., 2012, MNRAS, 421, 1671
Bouché N., Hohensee W., Vargas R., Kacprzak G. G., Martin C. L., Cooke J., Churchill C. W., 2012, MNRAS, 426, 801
Brooks A. M., Governato F., Quinn T., Brook C. B., Wadsley J., 2009, ApJ, 694, 396
Bruzual G., Charlot S., 2003, MNRAS, 344, 1000
Bryan G. L., Norman M. L., 1998, ApJ, 495, 80

Ceverino D., Dekel A., Bournaud F., 2010, MNRAS, 404, 2151
Chabrier G., 2003, PASP, 115, 763
Chen H.-W., Lanzetta K. M., Webb J. K., 2001, ApJ, 556, 158
Chen H.-W., Kennicutt R. C., Jr, Rauch M., 2005, ApJ, 620, 703
Chen H.-W., Helsby J. E., Gauthier J.-R., Shectman S. A., Thompson I. B., Tinker J. L., 2010, ApJ, 714, 1521
Churchill C., Steidel C., 2003, Rosenberg J. L., Putman M., eds, The IGM/Galaxy Connection: The Distribution of Baryons at z = 0. Vol. 281. Kluwer, Dordrecht, p. 149
Churchill C. W., Vogt S. S., 2001, AJ, 122, 679
Churchill C. W., Rigby J. R., Charlton J. C., Vogt S. S., 1999, ApJS, 120, 51
Churchill C. W., Mellon R. R., Charlton J. C., Jannuzi B. T., Kirhakos S., Steidel C. C., Schneider D. P., 2000, ApJS, 130, 91
Churchill C. W., Vogt S. S., Charlton J. C., 2003, AJ, 125, 98
Churchill C. W., Kacprzak G. G., Steidel C. C., 2005, in Williams P. R., Shu C.-G., Ménard B., eds, Proc. IAU Colloq. 199, Probing Galaxies through Quasar Absorption Lines. Cambridge Univ. Press, Cambridge, p. 24
Churchill C. W., Kacprzak G. G., Steidel C. C., Evans J. L., 2007, ApJ, 661, 714
Churchill C. W., Kacprzak G. G., Nielsen N. M., Steidel C. C., Murphy M. T., 2012a, ApJ, submitted
Churchill C. W. et al., 2012b, ApJ, 760, 68
Coil A. L. et al., 2011, ApJ, 743, 46
Cooksey K. L., Prochaska J. X., Chen H.-W., Mulchaey J. S., Weiner B. J., 2008, ApJ, 676, 262
Cooper M. C. et al., 2006, MNRAS, 370, 198
D'Agonstini G., 2000, preprint (arXiv:physics/0403086)
D'Agonstini G., Raso M., 2000, preprint (arXiv:physics/0002056)
Davé R., Hernquist L., Katz N., Weinberg D. H., 1999, ApJ, 511, 521
Dekel A., Birnboim Y., 2006, MNRAS, 368, 2
Dekel A. et al., 2009, Nat, 457, 451
Ding J., Charlton J. C., Churchill C. W., 2005, ApJ, 621, 615
Dixon W. V. et al., 2010, Cosmic Origins Spectrograph Instrument Handbook, Version 3.0. STScI, Baltimore, MD
Draine B. T., 2011, Physics of the Interstellar and Intergalactic Medium. Princeton Univ. Press, Princeton, NJ, p. 8 (ISBN: 978-0-691-12214-4)
Erb D. K., Steidel C. C., Shapley A. E., Pettini M., Reddy N. A., Adelberger K. L., 2006, ApJ, 646, 107
Faucher-Giguère C.-A., Kereš D., Ma C.-P., 2011, MNRAS, 417, 2982
Ferland G. J. et al., 1998, PASP, 110, 761
Fumagalli M. et al., 2011, MNRAS, 418, 1796
Haardt F., Madau P., 2012, ApJ, 760, 68
Jannuzi B. T. et al., 1998, ApJS, 118, 1
Kacprzak G. G., Churchill C. W., 2011, ApJ, 743, L34
Kacprzak G. G., Churchill C. W., Steidel C. C., Murphy M. T., 2008, AJ, 135, 922
Kacprzak G. G., Churchill C. W., Ceverino D., Steidel C. C., Klypin A., Murphy M. T., 2010a, ApJ, 711, 533
Kacprzak G. G., Murphy M. T., Churchill C. W., 2010b, MNRAS, 406, 445
Kacprzak G. G., Churchill C. W., Barton E. J., Cooke J., 2011a, ApJ, 733, 105
Kacprzak G. G., Churchill C. W., Evans J. L., Murphy M. T., Steidel C. C., 2011b, MNRAS, 416, 3118
Kacprzak G. G., Churchill C. W., Nielsen N. M., 2012, ApJ, 760, L7
Kereš D., Katz N., Weinberg D. H., Davé R., 2005, MNRAS, 363, 2
Kereš D., Katz N., Fardal M., Davé R., Weinberg D. H., 2009, MNRAS, 395, 160
Kriss G. A., 2011, COS Instrument Handbook 2011-01. STScI, Baltimore, MD
Mancone C. L., Gonzalez A. H., 2012, PASP, 124, 606
Martin C. L., Bouché N., 2009, ApJ, 703, 1394
Martin C. L. et al., 2012, preprint (arXiv:1206.5552)
McGaugh S. S., 2005, ApJ, 632, 859
Moster B. P. et al., 2010, ApJ, 710, 903
Nestor D. B., et al., 2011, MNRAS, 412, 1559
Noterdaeme P., Srianand R., Mohan V., 2010, MNRAS, 403, 906
Ocvirk P., Pichon C., Teyssier R., 2008, MNRAS, 390, 1326
Oppenheimer B. D. et al., 2010, MNRAS, 406, 2325
Péroux C., Bouché N., Kulkarni V. P., York D. G., Vladilo G., 2011, MNRAS, 410, 2237
Prochaska J. X., 2006, ApJ, 650, 272
Prochter G. E., Prochaska J. X., O'Meara J. M., Burles S., Bernstein R. A., 2010, ApJ, 708, 1221
Rao S. M., Turnshek D. A., Nestor D. B., 2006, ApJ, 636, 610
Ribaudo J. et al., 2011, ApJ, 743, 207
Rigby J. R., Charlton J. C., Churchill C. W., 2002, ApJ, 565, 743
Rubin K. H. R., et al., 2010, ApJ, 719, 1503
Rubin K. H. R., Prochaska J. X., Koo D. C., Phillips A. C., 2012, ApJ, 747, L26
Savage B. D., Sembach K. R., 1991, ApJ, 379, 245
Savaglio S. et al., 2005, ApJ, 635, 260
Schaye J., Carswell R. F., Kim T.-S., 2007, MNRAS, 379, 1169
Schlegel D. J., Finkbeiner D. P., Davis M., 1998, ApJ, 500, 525
Sijacki D., Vogelsberger M., Keres D., Springel V., Hernquist L., 2012, MNRAS, 424, 2999
Simard L. et al., 2002, ApJS, 142, 1
Skrutskie M. F. et al., 2006, AJ, 131, 1163
Steidel C. C., Sargent W. L. W., 1992, ApJS, 80, 1
Steidel C. C., Dickinson M., Persson S. E., 1994, ApJ, 437, L75
Steidel C. C., Kollmeier J. A., Shapely A. E., Churchill C. W., Dickinson M., Pettini M., 2002, ApJ, 570, 526
Steidel C. C. et al., 2010, ApJ, 717, 289
Stewart K. R., 2011, preprint (arXiv:1109.3207)
Stewart K. R., Bullock J. S., Wechsler R. H., Maller A. H., 2009, ApJ, 702, 307
Stewart K. R. et al., 2011a, ApJ, 735, L1
Stewart K. R. et al., 2011b, ApJ, 738, 39
Thom C. et al., 2011, ApJ, 736, 1
Tremonti C. A., Moustakas J., Diamond-Stanic A. M., 2007, ApJ, 663, L77
Tripp T. M. et al., 2005, ApJ, 619, 714
Tumlinson J. et al., 2011, Sci, 334, 948
van de Voort F., Schaye J., 2012, MNRAS, 423, 2991
van de Voort F., Schaye J., Booth C. M., Haas M. R., Dalla Vecchia C., 2011, MNRAS, 414, 2458
Weiner B. J. et al., 2009, ApJ, 692, 187
Wiersma R. P. C., Schaye J., Smith B. D., 2009, MNRAS, 393, 99
Zibetti S., Ménard B., Nestor D. B., Quider A. M., Rao S. M., Turnshek D. A., 2007, ApJ, 658, 161
Zonak S. G., Charlton J. C., Ding J., Churchill C. W., 2004, ApJ, 606, 196

This paper has been typeset from a TEX/LATEX file prepared by the author.